Modal detection for non-uniform thickness beams using continuous strain sensors and a strain-energy-based orthogonality condition

D.K. Anthony

Instituto de Acústica, Consejo Superior de Investigaciones Científicas (CSIC), C/ Serrano 144, 28006 Madrid, Spain

Abstract

Modal detection of regular-shape uniform thickness beams and plates using polyvinylidene fluoride (PVDF) sensors has been widely reported, especially related to active structural acoustic control. Here the application of PVDF sensors to a simply supported non-uniform thickness beam for modal detection is considered. As traditional kinetic-energy-based orthogonality conditions, based on displacement or temporal derivatives, are not applicable a new (approximate) strain-energy-based orthogonality condition is developed. Modal sensors are designed using one-dimensional (1-D) models of the beam and PVDF sensor, and then their performance is fully modelled in 2-D. Generally good modal discrimination is found but errors were significant for the two lowest modes. The effects of modelling and implementation errors were studied. An experimental modal sensor produced good agreement. Comprehensive details of the experimental system are given, especially with respect to the preparation of the PVDF sensors. Finally, the disadvantages of using strain sensors over other types of sensing are discussed, and it is shown that the new orthogonality condition cannot be extended to non-uniform plates.

1. Introduction

The application of polyvinylidene fluoride (PVDF) strain sensors to plates or beams in flexion has been widely studied. One of the most recent motivations has been the application of active structural acoustic control (ASAC). Here the acoustic radiation of a plate can be related through so-called radiation modes through specific combinations of structural modal amplitudes, and the task becomes a simultaneous detection of modal combinations. PVDF sensors are continuous sensors and thus avoid spatial aliasing problems. The width of a sensor strip can be varied along its length to achieve the required spatial sensitivity. In this way the output signal only requires a suitable amplifier alleviating the need for further signal processing. Examples of two approaches of designing PVDF sensors for ASAC are described by Fuller et al. [1] and Tanaka et al. [2].

E-mail address: iaca344@ia.cetef.csic.es

In this area, the analytical treatment is almost exclusively performed using the second spatial derivative of the plate (or beam) displacement. This is because for a uniform thickness plate the second spatial derivative can be easily related to the surface strain. For convenience the response of the PVDF sensor is also usually described in these terms for application to uniform thickness plates, although fundamentally it measures surface strain. When considering a non-uniform thickness beam the surface strain cannot be so conveniently represented. However, if a beam has a non-uniformity that is a step change in thickness over part of its length it could be considered uniform outside the region local to the step. The analytical development here is performed both in terms of second-order spatial derivatives and more generally in terms of the internal strains within the beam.

The Rayleigh–Ritz method solves for a series of basis functions to achieve an eigensolution for a simply supported beam and was previously considered by the author [3] for this type of problem. Due to the discontinuities in beam thickness a large number of basis functions were needed and this was the cause of an overshoot phenomenon in the apparent surface strain in the region of the discontinuity that is similar to Gibb's phenomenon. This caused spurious variations in the PVDF sensor width in these regions.

Clark and Burke [4] considered the practical aspects of applying such sensors. One result was that small sensor placement errors can lead to errors in the sensor response. This can be one possible cause of experimental frequency responses containing glitches or deviations from modelled results. In most cases reported in the literature when applying PVDF sensors to beams, the beam is considered to be a one-dimensional (1-D) system and thus only a 1-D model of the sensor is necessary. The present author uses a 2-D model for the beam and considers the error in using a 1-D model for the sensor. This is important if a practical system is to be accurately modelled.

To the author's knowledge this is the first time that a strain-energy-based orthogonality condition for modal detection on a non-uniform thickness beam using a PVDF sensor has been reported. Comprehensive details are also given on the application of the beam system, especially the sensors, as little information is generally given in the literature on the use of PVDF, which has many practical issues in its application.

The article is structured as follows. Section 2 recapitulates orthogonality and develops the strain-energy-based orthogonality condition. Section 3 deals with appropriate models for the PVDF sensor, and Section 4 details how PVDF sensors are designed for modal detection based on the new orthogonality condition. Section 5 details the numerical model, and in Section 6 numerical results for the detection of different modes are given. Section 7 details the experimental system and in Section 8 the results of an experimental implementation of a modal sensor are given. Section 9 discusses issues arising from the reported work and its application. The work is concluded in Section 10. Appendix A is given for the derivation of the modal excitation of a non-uniform thickness plate by piezoelectric actuators.

2. Orthogonality

In the vibration of plates, shells and beams, any linear vibration distribution can be considered to be the sum of a series of eigenfunctions (mode shapes) each having a natural response at their corresponding eigenvalues (*modal* or *natural frequencies*). Solution of the mode shapes and natural frequencies is only possible on a theoretical basis for a handful of simple cases. Otherwise numerical methods, often involving dividing the structure into a small number of elements, are required.

2.1. Kinetic-energy-based orthogonality

An important property of an energy conservative system is that orthogonality exists mutually between all mode shapes having distinct natural frequencies (which is usually the case). If the mth and nth mode shapes of a plate of area S are denoted φ_m and φ_n, then the orthogonality is stated by [5]

$$\int_S m'' \varphi_m \varphi_n \, \mathrm{d}S = \begin{cases} 0 & m \neq n, \\ \Lambda_m & m = n, \end{cases} \tag{1}$$

where m'' is the plate mass area density and Λ_m is the modal mass. This provides a simple expression that is directly applicable to systems measuring the transverse displacement (or the time derivatives of velocity or acceleration). It should be noted that the orthogonality condition is normally given for uniform plates where the mass distribution is constant and m'' can be excluded from the definition. However, for non-uniform plates (non-uniform thickness or material) the mass distribution must be included to achieve correct independent modal detection. A consequence of orthogonality is modal independence. This is demonstrated by considering the kinetic energy of a plate due to either mode m or mode n in isolation, which are given by

$$\text{KE}_m = \frac{1}{2}\int_S m''v_m^2\varphi_m^2\,\mathrm{d}S, \quad \text{KE}_n = \frac{1}{2}\int_S m''v_n^2\varphi_n^2\,\mathrm{d}S, \qquad (2\text{a,b})$$

where v_m and v_n the transverse velocity amplitudes. When both modes exist simultaneously and are mutually independent, the total vibrational energy is the sum of the individual energies, KE_m and KE_n, to ensure conservation of energy. So

$$\text{KE}_{m+n} = \frac{1}{2}\int_S m''(v_m\varphi_m + v_n\varphi_n)^2\mathrm{d}S = \text{KE}_m + \text{KE}_n. \qquad (3\text{a,b})$$

The resulting cross product will be zero when $m \neq n$ confirming modal independence as a consequence of the orthogonality condition (1).

2.2. Strain-energy-based orthogonality

Two derivations of the strain-energy-based orthogonality condition are given here. The first relates to the common expressions of the strain energy of a plate and the response of a PVDF sensor using second spatial derivatives. This is directly applicable to the use of the Rayleigh–Ritz analysis for the beam solution. The second is based on the surface strain of a plate, and is applicable to the use of finite element analysis (FEA). In both cases an approximation is made that the only significant beam bending occurs along the beam length for the modes of interest. This assumption is validated numerically in Section 6.1.

2.2.1. Orthogonality condition based on second spatial derivative

The maximum potential energy, U_p (through strain) of a plate of dimensions (L_x, L_y) undergoing vibration is given in many standard texts (for example Ref. [6]). It may be adapted for application to non-uniform plates as

$$U_P = \frac{1}{2}\int_0^{L_y}\int_0^{L_x} D(x,y)\left(\left(\frac{\partial^2 W}{\partial x^2}\right)^2 + \left(\frac{\partial^2 W}{\partial y^2}\right)^2 + 2v(x,y)\left[\frac{\partial^2 W}{\partial x^2}\frac{\partial^2 W}{\partial y^2} + 2(1-v(x,y))\left(\frac{\partial^2 W}{\partial x \partial y^2}\right)\right]\mathrm{d}x\,\mathrm{d}y\right), \quad (4)$$

where W is the transverse plate displacement, v is Poisson's ratio. The plate bending rigidity, D, for a non-uniform plate is defined as

$$D(x,y) = \frac{E(x,y)h^3(x,y)}{12(1-v(x,y)^2)}, \qquad (5)$$

where E is the Young's modulus of the plate and h is the plate thickness. It is assumed here that all changes in thickness are plane symmetric about the mid-surface plane of the beam, which is also the neutral bending plane. Although valid for gradual variations in thickness (for example, a tapered beam) Eq. (4) is unlikely to be valid in the region of a discontinuity in thickness as it assumes that strain and stress vary linearly in the z-direction. This is discussed in more detail below.

Using the same derivation method as above, relying on modal independence, a four term "orthogonality condition" results [3]. The equality to zero could be met by combinations of non-zero components and does not allow a one-term orthogonality condition, for application along the sensor length, to be derived. Considering the beam as a 1-D beam system the beam displacement can be expressed as the sum of a series of 1-D spatial modes so that the displacement is constant in the direction of the y-axis. In this way the strain

energy in the beam can be approximated as

$$U_P \approx \frac{1}{2} \int_0^{L_y} \int_0^{L_x} D(x,y) \left(\frac{\partial^2 W}{\partial x^2} \right)^2 dx\, dy. \tag{6}$$

The modal independence described above also applies to the strain energy of each mode and this allows a strain-energy-based orthogonality condition that has practical application as it can be defined using one term alone:

$$\int_0^{L_x} D(x) \frac{\partial^2 \phi_m}{\partial x^2} \frac{\partial^2 \phi_n}{\partial x^2} dx \approx \begin{cases} 0 & m \neq n, \\ \Lambda_m^D & m = n. \end{cases} \tag{7}$$

where Λ_m^D is the modal stiffness. If the non-uniform beam is homogenous (only has variable beam thickness) the condition can be more simply expressed as

$$\int_0^{L_x} h^3(x) \frac{\partial^2 \phi_m}{\partial x^2} \frac{\partial^2 \phi_n}{\partial x^2} dx \approx \begin{cases} 0 & m \neq n, \\ \Lambda_m^h & m = n. \end{cases} \tag{8}$$

2.2.2. Orthogonality condition based on surface strain

The strain energy of a plate or beam in flexion can also be directly expressed in terms of the internal plate strains and stresses [7]

$$U_P = \frac{1}{2} \int_0^{L_x} \int_0^{L_y} \int_{-h(x)/2}^{+h(x)/2} (\sigma_x \varepsilon_x + \sigma_y \varepsilon_y + \sigma_z \varepsilon_z + \tau_{xy} \gamma_{xy} + \tau_{xz} \gamma_{xz} + \tau_{yz} \gamma_{yz})\, dz\, dy\, dx, \tag{9}$$

where σ_x, σ_y, σ_z and ε_x, ε_y, ε_z represent the stress and strain components in the coordinate directions indicated in the subscripts, and τ_{xy}, τ_{xz}, τ_{yz} and γ_{xy}, γ_{xz}, γ_{yz} represent the shear stresses and strains using the common convention given in Ref. [7]. Here it is also stated that for thin plates σ_z, γ_{xz}, γ_{yz} can be regarded as insignificant and their corresponding product terms removed. Using the following identities:

$$\sigma_x = \frac{E}{1 - v^2}(\varepsilon_x + v\varepsilon_y), \quad \sigma_y = \frac{E}{1 - v^2}(\varepsilon_y + v\varepsilon_x), \quad \tau_{xy} = G\gamma_{xy}, \tag{10}$$

where G is the shear modulus, which is equal to $E/2(1 + v)$, the strain energy can be expressed in terms of normalised strain components as

$$U_P = \frac{E}{2(1 - v^2)} \int_0^{L_x} \int_0^{L_y} \int_{-h(x)/2}^{+h(x)/2} \left[\varepsilon_x^2 + \varepsilon_y^2 + 2v\varepsilon_x \varepsilon_y + \frac{1 - v}{2} \gamma_{xy}^2 \right] dz\, dy\, dx. \tag{11}$$

Each term taken in order corresponds directly to those in Eq. (4). As with the derivation based on the second spatial derivative, for lower order modes a good approximation of the strain energy can be obtained using just the x-strain term along the beam length

$$U_p \approx \frac{L_y E}{2(1 - v^2)} \int_0^{L_x} \int_{-h(x)/2}^{h(x)/2} [\varepsilon_x(x,y)]^2\, dz\, dx. \tag{12}$$

For application to a sensor that measures the surface strain of the beam, ε^s, the strain energy can be expressed in such terms as

$$U_p \approx \frac{L_y E}{2(1 - v^2)} \int_0^{L_x} [\varepsilon_x^s(x)]^2 g_{<M>}(x)\, dx. \tag{13}$$

$g_{<M>}$ is a generic weighting function where M denotes the method of calculation. If it is assumed that the strain varies linearly with z, as is the case away from discontinuities in h (see Fig. 1) then,

$$\varepsilon_x(x,z) = \frac{2\varepsilon_x^s(x)z}{h(x)} \Bigg|_{|z| \leqslant h(x)/2} \tag{14}$$
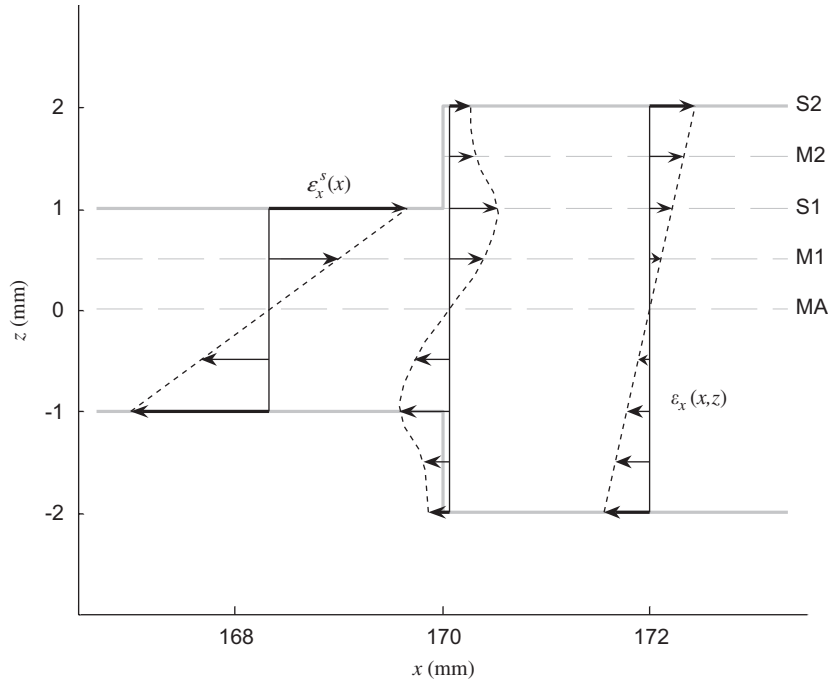
Fig. 1. Cross-section of the beam considered (see Fig. 2) in the vicinity of one of the discontinuities in thickness showing (i) the definition of the internal and surface layers used in the analysis of the beam, and (ii) the variation of strain with z away from and in the immediate vicinity of the discontinuity when in flexion. Data taken from beam mode (3,1,0).

and the weighting function, g_h, can be seen to be

$$g_h(x) = \tfrac{1}{3}h(x). \tag{15}$$

However, it is demonstrated in Fig. 1 that the strain does not vary linearly with z near discontinuities in thickness. A more comprehensive weighting function, g_n, can be defined that is the strain energy normalised to the surface strain squared as a function of x, and is

$$g_n(x) = \frac{\int_{-h(x)/2}^{h(x)/2}[\varepsilon_x(x,z)]^2\,\mathrm{d}z}{[\varepsilon_x^s(x)]^2}. \tag{16}$$

g_n is expected to be identical to g_h away from discontinuities in thickness. Similar variations in stress with z as with strain are also seen. In practice g_n is ambiguous at discontinuities but can be evaluated fractionally either side of a discontinuity so as to distinguish the values on the thin and thick beam sections "at" this point.

An orthogonality condition can be derived in terms of the surface strain, by considering two modal strain contributions from modes m and n of amplitudes A_m and A_n, respectively,

$$\varepsilon_x^s(x) = A_m\phi_m^s(x) + A_n\phi_n^s(x), \tag{17}$$

where ϕ^s is a strain mode shape. This is the strain field in the x-direction due to the corresponding normalized (displacement) mode shape. Modal independence was established above, and so both modal contributions must equal the sum of the individual values of the modal strain energy and the following orthogonality condition results:

$$\int_0^{L_x} g_{<M>}(x)\,\phi_m^s(x)\phi_n^s(x)\,\mathrm{d}x \approx \begin{cases} 0 & m \neq n, \\ \Lambda_m^s & m = n. \end{cases} \tag{18}$$

If both the stress and strain are available, as is the case here from FEA analysis, a potentially more accurate weighting function can be calculated as

$$g_{\sigma\varepsilon}(x) = \frac{\int_{-h(x)/2}^{h(x)/2} \sigma_x(x,z)\varepsilon_x(x,z)\,\mathrm{d}z}{[\varepsilon_x^s(x)]^2}. \tag{19}$$

The differences in using g_h, g_n and $g_{\sigma\varepsilon}$ are studied below. In the following $g_{\langle M\rangle}$ will be used to denote a generic weighting function that could be any of these three. It is noted that the use of the normalised strain is required to derive the orthogonality condition.

2.2.3. Equivalence of the two strain-energy-based orthogonality conditions

The orthogonality conditions given above in Eqs. (8) and (18) are both derived from consideration of the strain energy, and are therefore equivalent. For analysis based on the second spatial derivatives, commonly used for application to uniform thickness plates, Eq. (8) is best suited, and states that the weighting function required is $h^3(x)$. If the surface strain is directly accessible, as with FEA, then g_n or $g_{\sigma\varepsilon}$ can be evaluated and these are expected to be proportional to $h(x)$ away from discontinuities in thickness. Recalling the 1-D approximate relation between the surface strain and the beam bending [7]

$$\varepsilon_x^2(x) = -z\left.\frac{\partial^2 W}{\partial x^2}\right|_{z=h(x)/2} \tag{20}$$

and its equivalent in terms of the bending and surface strain modes is

$$\phi_m^s(x) \propto h(x)\frac{\partial^2 \phi_m}{\partial x^2}. \tag{21}$$

Substituting Eq. (21) into Eq. (18) the orthogonality condition (8) results (for x away from discontinuities in $h(x)$).

3. Polyvinylidene fluoride strain sensors

The use of surface applied sensors to measure plate flexion through surface strain is commonplace, in particular sensors employing PVDF. PVDF is a thin flexible sheet whose shape can be conveniently formed to provide an appropriate weighting function. Its use for sensing plate vibration has been well reported [4,8,9]. The surface strain of a plate in flexion can be related to the second-order spatial derivative of the plate displacement, and when applying PVDF sensors to uniform thickness plates this is the parameter commonly used; however it may also be defined more simply and directly in terms of the surface strain. For this reason the study of non-uniform thickness plates here begins in terms of the spatial derivatives.

The response of a PVDF sensor strip applied, at $y = y_s$ to a beam of length L_x and width L_y, with respect to its transverse vibratory movement is given by a change of charge, $q(t)$, between its electrode surfaces as [3]

$$q(t) \approx \mathrm{e}^{\mathrm{j}\omega t}\frac{1}{2}\int_0^{L_x}\int_{y_s-bS(x)}^{y_s+bS(x)} h(x)\left(e_{31}^0\frac{\partial^2 W}{\partial x^2} + e_{32}^0\frac{\partial^2 W}{\partial y^2}\right)\mathrm{d}y\,\mathrm{d}x. \tag{22}$$

where W the displacement field of the plate, e_{31}^0 and e_{32}^0 are the charge constants of the PVDF. It is assumed that the skew/cross-axis sensitivity (e_{36}^0) is zero [3] and the sensor thickness is much smaller than h. The sensor has a width profile function of $S(x)$ and a corresponding scaling factor b. The height function h is incorporated inside the integral as it is a function of x for a non-uniform thickness plate and it provides a natural spatial sensor weighting in addition to $S(x)$. For dominant bending in the x-direction a simplified 1-D model of this sensor can be used:

$$q(t) \approx \mathrm{e}^{\mathrm{j}\omega t}e_{31}^0 b\int_0^{L_x} S(x)h(x)\frac{\partial^2 W}{\partial x^2}\,\mathrm{d}x. \tag{23}$$

The response is more fundamentally expressed in terms of the surface strain of the plate [10], in this case

$$q(t) \approx e^{j\omega t} \int_0^{L_x} \int_{y_s - bS(x)}^{y_s + bS(x)} \left(e_{31}^0 \varepsilon_x^s(x) + e_{32}^0 \varepsilon_y^s(y) \right) dy \, dx, \tag{24}$$

where ε_x^S and ε_y^S are the surface strain of the plate in the x- and y-directions, respectively. As above, for a 1-D consideration, the response be simplified to

$$q(t) \approx 2e^{j\omega t} e_{31}^0 b \int_0^{L_x} S(x) \varepsilon_x^s(x) \, dx. \tag{25}$$

Apart from regions near discontinuities in beam thickness, Eqs. (23) and (25) are equivalent.

4. Sensor design

Using the expressions for the strain energy of the beam and the single term orthogonality condition, a PVDF sensor can be designed for modal detection. The design is defined by the shape function, $S(x)$, which defines the width profile of the sensor along its length. It is noted that the design can only proceed using the approximate 1-D orthogonality condition and a 1-D consideration of the PVDF sensor. Thus a 1-D beam model is used to describe the displacement, W, as a sum of 1-D spatial modes ϕ_m and corresponding modal amplitudes A_m as

$$W(x) = \sum_m A_m \phi_m(x). \tag{26}$$

However, later on the numerical model will allow the complete PVDF response to be predicted and the error in using the 1-D model to be evaluated.

4.1. Design based on second-order spatial derivative

A sensor width profile can be defined to detect mode d independently. For a non-uniform thickness beam the width profile $S_D(d,x)$ is a function of the second-order spatial derivative of the desired mode, ϕ_d, and the height function of the beam

$$S_D(d, x) = h^2(x) \frac{\partial^2 \phi_d}{\partial x^2}. \tag{27}$$

The charge output of the sensor can be obtained by substituting Eqs. (26) and (27) into Eq. (23) and applying the orthogonality condition (8)

$$q_d(t) \approx A_d e^{j\omega t} e_{31}^0 b \Lambda_m^h. \tag{28}$$

Thus a factor equal to the square of the height profile must be included in the sensor width profile to supplement the factor h that is naturally included in applying the PVDF sensor to the surface of a beam with variable thickness.

4.2. Design based on surface strain

Using the generic notation above whereby the sensor design method is defined as $M = \{h, n, \sigma\varepsilon\}$, the corresponding width profiles S_M are defined as functions of the surface strain of the desired mode, ϕ_d^s, and the appropriate weighting functions as

$$S_M(d, x) = g_M(x) \phi_d^s(x), \tag{29}$$

which similarly leads to the detection of the amplitude of the desired mode:

$$q_d(t) \approx A_d e^{j\omega t} e_{31}^0 b \Lambda_m^s. \tag{30}$$

In both Eqs. (28) and (30) approximation equalities are used as they are based on 1-D approximations of the strain energy of the beam, the corresponding orthogonality conditions, and a 1-D model of the PVDF sensor.

5. Numerical model of beam system

The non-uniform thickness beam considered in this paper, shown in Fig. 2, is made of stainless steel and has dimensions $380 \times 40 \, \text{mm}^2$. The nominal thickness is 2 mm, but over a 40 mm region in the beam centre the thickness is augmented to twice-thickness (4 mm). The beam is symmetric about its mid-surface, and is simply supported at both ends. The beam system was modelled as a 3-D system using FEA package (ANSYS [11]) and subsequently in 2-D in MATLAB [12]. Even though the system is a 1-D system to a first-order approximation, a 1-D model is not sufficiently accurate. The combination of free–free boundary conditions (on the long parallel edges of the beam) and a finite Poisson's ratio causes significant curvature of the displacement contours across the beam width. This is evident in Fig. 2 where the displacement field for mode (3,1,0) is given as an example.

A block diagram of the numerical model is shown in Fig. 3, and this is now discussed. The displacement modes and corresponding surface strain modes are calculated using a finite element model. The beam was meshed using element SOLID 45 in 0.5 mm thick layers. The width of the beam was divided into 20 elements. Two-millimeter mesh divisions were used in the x-direction over the majority of the beam length. Over a section 20 mm from the change of thickness the mesh was linearly increased to 1 mm, and 1 mm divisions were used in the central region. The beam material properties were: $E = 200 \times 10^9 \, \text{N/m}^2$, $v = 0.28$, $\rho = 7800 \, \text{kg/m}^3$. First a modal analysis was performed to solve for the natural frequencies of the system, then using a unit driving force at each natural frequency and harmonic analysis, both displacement and strain mode shapes are determined.

These mode shapes are further processed in MATLAB. The modes are re-sampled to an even grid of 761×81, giving a resolution of about 0.5 mm in each axis. For given piezoceramic actuator positions a modal model is used to calculate the modal excitation in terms of displacement modal amplitudes. The displacement modal amplitudes are calculated similarly as shown by Dimitriadis et al. [13], but in this case a non-uniform thickness beam is used and a more general expression is derived in Appendix A. The modal amplitudes, A_{mn} (for mode order m, n), are based on Eq. (A.15) and are

$$A_{mn} = \frac{C_0 \varepsilon_{\text{pe}} [G_{mn}^x(x_1, x_2) + G_{mn}^y(y_1, y_2)]}{\Lambda_{mn}(\omega_{mn}^2 - \omega^2 + 2\text{j}\xi_{mn}\omega_{mn}\omega)}, \tag{31}$$

where C_0 and ε_{pe} are piezoelectric coupling term and the induced piezoelectric strain, ω_{mn} is the modal frequency, and x_1, x_2, y_1, y_2 define the limits of the actuator. Here modal damping has been added in the denominator, and a value of modal damping, ζ_{mn}, of 0.008 was found to provide good agreement with the experiment measurements subsequently presented, and was used in the model. The modal mass Λ_{mn} is defined in Eq. (A.16), and G_{mn}^x and G_{mn}^y are:

$$G_{mn}^x(x_1, x_2) = \int_{x_1}^{x_2} \left(\frac{\partial \phi_{mn}(x, y_2)}{\partial y} - \frac{\partial \phi_{mn}(x, y_1)}{\partial y} \right) \text{d}x, \quad G_{mn}^y(x_1, x_2) = \int_{y_1}^{y_2} \left(\frac{\partial \phi_{mn}(x_2, y)}{\partial x} - \frac{\partial \phi_{mn}(x_1, y)}{\partial x} \right) \text{d}y. \tag{32}$$
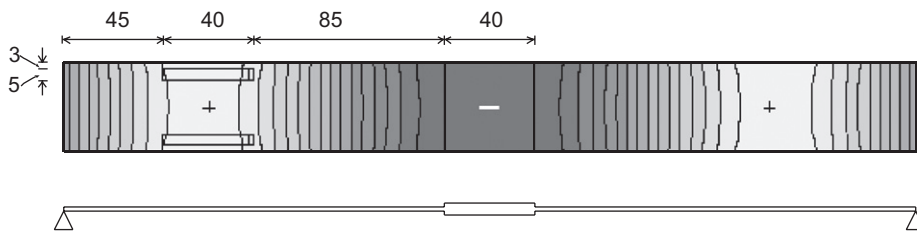

Fig. 2. Details of the beam system considered comprising of a simply supported stainless steel beam of dimensions $380 \times 40 \, \text{mm}^2$. The nominal thickness is 2 mm except in the central region where the thickness is 4 mm. The position of the actuators is also shown. The contour lines show the displacement field associated with mode (3,1,0).
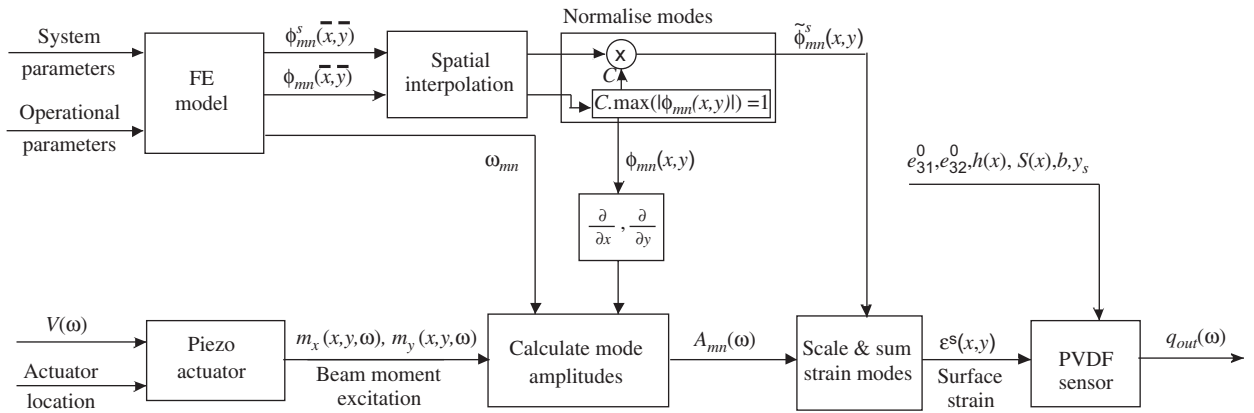
Fig. 3. A schematic diagram of the complete numerical model used to estimate the PVDF sensor charge output of the beam system from the beam actuator excitation signal V. The symbols are defined in the text.

The amplitudes A_{mn} are used to scale the strain modes and their sum is thus the net surface strain across the beam surface in the x and y axes directions (ε_x and ε_y). The response of the PVDF sensor is then calculated by overlaying the sensor shape on the strain fields, and a numerical integration, based on Eq. (24), performed over the area of the sensor. The calculated charge output at each frequency is

$$q(t) = \sum_{0 \leqslant x_m \leqslant L_x} \sum_{\substack{y_s - b|S(x)| \\ \leqslant y_n \leqslant y_s + b|S(x)|}} \text{sgn}(S(x_m))(e^0_{31}\varepsilon^s_x(x_m) + e^0_{32}\varepsilon^s_y(y_n))s(x_m, y_n), \tag{33}$$

where x_m and x_n define the positions of the element centres of the surface grid elements, and s is the fraction of each element that falls within the sensor outline. For elements completely inside the profile s will be unity, but on the sensor border fractional values allow greater accuracy without the necessity of increasing the beam surface quantisation. The signum operator ensures the correct polarity of the individual charge elements according to $S(x)$. This sensor model allows the complete response of the PVDF sensor to be modelled, including its cross-axis response, even though the premise of the sensor design assumes a unidirectional response.

It is noted that when using a Rayleigh–Ritz model, the model architecture differs. The displacement modes are scaled and summed to produce a net displacement field, this is then converted into $\partial^2 W/\partial x^2$ and $\partial^2 W/\partial y^2$ fields. A numerical version of Eq. (22) would then be used to calculate the response of the sensor.

6. Numerical results using beam system model

The numerical model was used to validate some of the assumptions made above and to predict the performance of a sensor design when applied to the beam surface. The first 11 eigenfrequencies of the non-uniform thickness beam resulting from the modal analysis are given in Table 1 along with the order of the mode shapes. The analysis was also performed for a 2 mm-thick uniform beam of the same dimensions for comparison. Note that at one frequency in each case a higher z mode order appears due to the beam moving in the z-plane. This mode did not result from the (2-D) Rayleigh–Ritz analysis [3]. In practice, the effect of these modes is likely to be minimal as the experimental implementation of the boundary conditions used here (and discussed later on) only provides frictional, and not positive, constraint the z-direction.

6.1. Validation of a single-term strain-energy orthogonality condition

In order to validate the assumption made above that the total strain energy of the beam could be approximated for low modal orders using only the strain-energy component in the x-direction, its proportion

Table 1
Modal frequencies and modal orders (in *x,y,z*) of the first 11 modes of the uniform and the non-uniform thickness beams considered. The proportion of strain energy in the *x*-axis to the total strain energy, α, for each mode is also shown

Mode	Uniform beam			Non-uniform beam		
	Freq (Hz)	Modal order	$\alpha(\phi_m^s)$	Freq (Hz)	Modal order	$\alpha(\phi_m^s)$
1	31.819	(1,1,0)	0.8115	32.259	(1,1,0)	0.8277
2	127.46	(2,1,0)	0.8168	127.49	(2,1,0)	0.8199
3	287.38	(3,1,0)	0.8249	303.02	(3,1,0)	0.8377
4	411.97	(1,2,0)	0.0066	374.82	(1,2,0)	0.0095
5	512.17	(4,1,0)	0.8345	513.03	(4,1,0)	0.8425
6	802.34	(5,1,0)	0.8448	863.50	(5,1,0)	0.8512
7	831.53	(2,2,0)	0.0258	946.35	(2,2,0)	0.0608
8	1158.3	(6,1,0)	0.8551	1164.7	(6,1,0)	0.8645
9	1266.0	(3,2,0)	0.0560	1203.9	(3,2,0)	0.0712
10	1330.6	(0,0,1)	0.4934	1229.5	(0,0,1)	0.4328
11	1580.2	(7,1,0)	0.8648	1719.4	(7,1,0)	0.8663

of the total strain energy, α, was calculated for each strain mode, *m*, as

$$\alpha(\phi_m^s) = \frac{L_y E}{6(1 - v^2)} \int_0^{L_x} [\phi_m^s(x)]^2 h(x) \, \mathrm{d}x / U_P(\phi_m^s(x, y, z)) \tag{34}$$

and this is included in Table 1. The strain energy was calculated from the surface strain components using the assumption of the strain being linearly dependent on *z*, as denoted in Eq. (14) for the *x*-axis component. It can be seen that for all the modes of order (*,1,0) (of order unity in the *y*-direction) the strain component in the *x*-direction accounts for 80–90% of the total strain energy, increasing with the modal order. The 2 mm thick uniform beam has similar characteristics.

6.2. Development of sensor design

The design of a sensor is now detailed using intermediate steps to demonstrate how the above theory is applied and also to allow some pertinent observations to be made. A sensor is designed to detect mode (*m*,1), and is termed a "mode-*m* sensor". Fig. 4 details the design of a mode-3 sensor. The displacement mode shape is shown and the effect of the thicker central section is obvious where reduced curvature occurs. The strain and stress on internal and surface planes (denoted in Fig. 1) along the beam are also shown around the region of one of the discontinuities in thickness. On the mid-surface (MA) zero values of strain and stress are seen, as expected. It is seen that away from the immediate region of the discontinuity the strain and stress appear to be linearly related to *z* (the distance from the mid-surface plane) in both the thinner and thicker sections. The strain and stress at levels M1 and S1 change over the step-like discontinuity in thickness in a smooth fashion. However, the strain and stress on the levels exclusive to the thicker section (M2 and S2) diminish as the discontinuity is approached, and are no longer linearly related to *z*. Careful examination also reveals small differences between the strain and stress functions, especially in the immediate region of the discontinuity. This is found to be more significant as the change in thickness increases. Hence calculating the energy from the normalised strain (see Eq. (16)) in the region of discontinuities may induce a small error.

The strain energy corresponding to mode-3 is also shown. The central thicker section corresponds to relatively small energy due to the reduced curvature. The maximum strain-energy density is seen in the thinner section either side of the thicker section emphasizing that accurate measurement in this region is important for good modal discrimination. A maximum value of strain energy is also seen in this location for other modes except where, due to the modal order, a minimum in the strain energy occurs over the central region.

Both weighting functions $g_n(x)$ and $g_{\sigma\varepsilon}(x)$ are next shown. These are normalised to unity in the mid-section of the thinner section of the beam, and are approximately a value of 2 (the value of g_h) in the centre region of
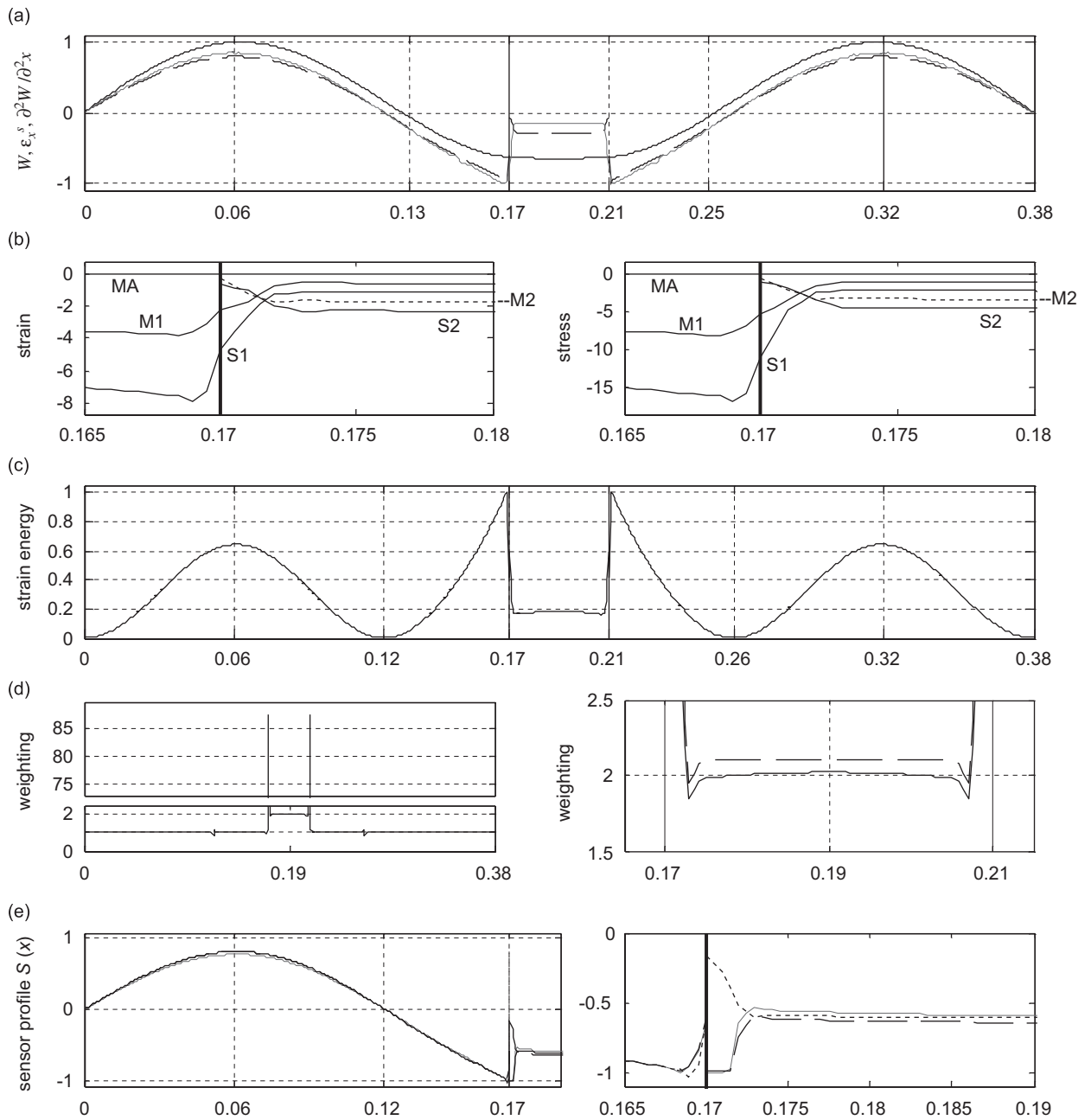
Fig. 4. The spatial variation of various variables (normalised where necessary) related to mode-3 of the non-uniform thickness beam, whose thicker section is between the limits $x = \{0.17, 0.21\}$. The independent axis is x in all cases: (a) the displacement W (—) surface strain (▬) and second-order spatial derivative of W (- - -); (b) the levels of strain and stress of the internal and surface layers defined in Fig. 1; (c) the distribution of the strain energy in the x-direction; (d) the weighting functions $g_{\sigma\varepsilon}$ (—) and g_n (- - -) with detail in the thicker section; and (e) the sensor width profile function along the beam and detail in the vicinity of a discontinuity in thickness for $S_{\sigma\varepsilon}^T$ (▬), S_n^T (- - -) and S_h ($\cdots$). All spatial variables are symmetric about the beam mid-length ($x = 0.19$ m).

the thicker section. However, as the surface strain in the thicker section diminishes towards the discontinuity in thickness this leads to a large spike in the weighting function exceeding a value of 85. Lastly in this figure, the profile of the sensors defined by $g_n(x)$ and $g_{\sigma\varepsilon}(x)$ are shown. In practice it is necessary to

use truncated versions of the sensors where the maximum value of the sensor tails at the edges of the thicker section are limited to the sensor width in the centre of this section ($x = 0.19$). These are also modelled and denoted $S_n^T(3, x)$ and $S_{\sigma\varepsilon}^T(3, x)$. The significance of this truncation is considered below. $S_h(3,x)$ is also shown, and this profile naturally diminishes towards the discontinuity and truncation is not necessary.

Finally, it is noted that the maximum values in the displacement mode shape, the strain-energy distribution and the width in the two outer sensor lobes all coincide at similar values of x. However, the nodal positions in the displacement mode shape do not correspond with the other two functions. One test of the integrity of the numerical model would be to confirm correct positioning of the modal nodes with an experimental system. This is much more easily done in terms of displacement but will not correspond with the zero-crossing points of the sensor width function $S(x)$.

6.3. Predicted modal discrimination

In order to predict the ability of a sensor in detecting only the desired mode when other modes exist, the *modal discrimination* can be calculated by evaluating the orthogonality integral. Exact modal orthogonality is not expected as the orthogonality condition is an approximate one and will also be further limited due to practical restrictions in the implementation. Although the detection is performed using the surface strain, it is necessary to normalise the mode shapes in terms of displacement as this is the parameter being determined (via the measurement of surface strain). The modal discrimination is considered for the three design methods, $M = \{h, n, \sigma\varepsilon\}$. The modal discrimination, O_M, of a sensor designed to detect mode d, and with sensor width profile $S_M(d,x)$, in the presence of the normalised strain mode $\tilde{\phi}_m^s$ is given by

$$O_M(d, m) = \frac{\int_0^{L_x} S_M(d, x)\tilde{\phi}_m^s(x)\, \mathrm{d}x}{\int_0^{L_x} S_M(d, x)\tilde{\phi}_d^s(x)\, \mathrm{d}x}. \tag{35}$$

Fig. 5 shows O expressed in decibels for sensors designed to individually detect the first five modes (mode-1 to mode-5) principally for sensor profile $S_{\sigma\varepsilon}^T$, but also for profiles $S_{\sigma\varepsilon}$ and S_h. A practical frequency range of interest would be typically less than 1 kHz, although a range of up to 5 kHz is shown so that a more complete picture of the modal discrimination is demonstrated. The x-axis shows each modal order $(m,1)$ located at the value of its modal frequency on a linear scale denoted at the top to enable the significance of errors to be seen with the proximity to the modal frequency. The modal frequencies for a uniform thickness beam are approximately proportional to the modal order squared. With reference to Table 1 this is only seen to be adhered to approximately for the non-uniform thickness beam. The range of O is limited to 60 dB as greater signal to noise ratios are not realisable in practical systems with a realistic noise floor. Furthermore, it is suggested that modal discrimination of about 40 dB is sufficient in many systems.

In the figure it is seen that for odd-mode sensors the greater errors are produced from the unwanted odd modes, and for even-mode sensors greater errors from unwanted even modes. For $S_{\sigma\varepsilon}^T(1, x)$ the greatest errors occur and the useful frequency range would have to be limited to about 500 Hz. The use of either $S_{\sigma\varepsilon}$ or S_h would not achieve any reasonable frequency range of useful modal discrimination. The discrimination of the mode-2 sensor also suffers from a similarly limited frequency range but is not so dependent upon the sensor design method. The mode-3 sensor, which is implemented later on, is seen to have reasonably good predicted modal discrimination up to about 3 kHz. It is seen that the higher the modal order of the sensor, in general the better the modal discrimination.

It is interesting to note that the truncation of the tails in the centre sensor section, whilst a deviation from the specified sensor design on practical grounds, has in general improved the discrimination. Also, for the mode-2 and mode-4 sensors it is seen that S_h provides significantly better discrimination. This is surprising as it is the most approximate method assuming a global linear strain-z relationship. However, the orthogonality condition is approximate, as discussed above, and the sensor designs are obviously not optimal. For the odd-mode sensors it is seen that $S_{\sigma\varepsilon}^T$ has the best general performance.
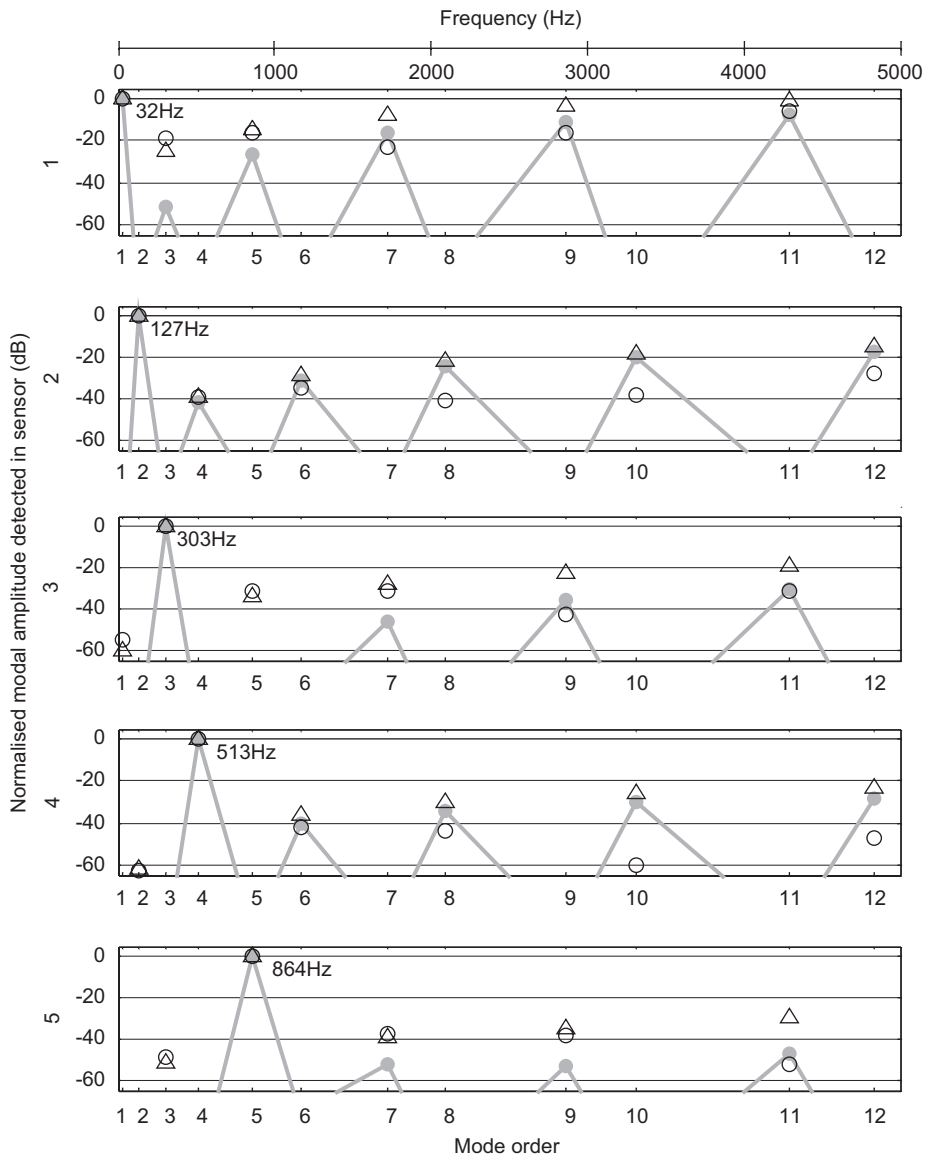
Fig. 5. The values of modal discrimination, O, for mode-1 to mode-5 sensors for the first 12 modes (*,1,0) with different sensor designs based on different sensor profile functions. Key: $S_{\sigma\varepsilon}^{T}$ (—●—), $S_{\sigma\varepsilon}$ (Δ) , S_h ($\circ$).

The above predicted sensor performance assumes a zero-width sensor that has no variation in $\partial^2 W/\partial x^2$ across its width, nor response to bending in this direction ($\partial^2 W/\partial y^2$), but implicitly implements the required weighting function $S(x)$ along its length. The significance of the assumption of such a sensor will be considered below when the numerical model and experimental results are presented. It is also a rather harsh prediction as all modes are considered to be of equal amplitude. However, in practice it is usually the case that the modal energy decreases with frequency. If the modal amplitudes are known then the actual amplitude of each modal (error) component detected by a sensor could be predicted, as shown for this beam arrangement in Ref. [3].

Finally, it is noted that the discrimination of sensors using the normalised strain (S_n and S_n^{T}) in general had worse performance than $S_{\sigma\varepsilon}^{T}$ and similar performance as $S_{\sigma\varepsilon}$. These were not included here for clarity, but S_n^{T} will be considered in the next section.
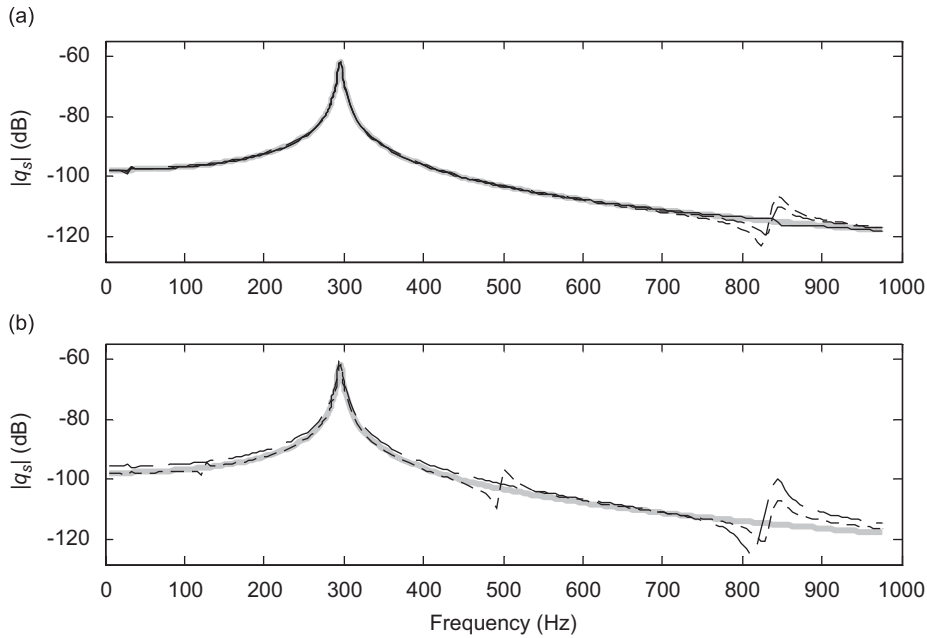
Fig. 6. A comparison of different predicted responses of mode-3 sensors with the true amplitude response of the third mode (▬▬): (a) sensor profiles $S^T_{\sigma\varepsilon}$ (——), S_n(- - -) and S_h (···); (b) a sensor having no cross-sensitivity (- - -) and for a sensor positioning error of -1.1 mm in x (···). (The true amplitude response is shown scaled for best fit with $S^T_{\sigma\varepsilon}$.)

6.4. Predicted mode-3 sensor response

Using the numerical model detailed above the frequency response of the mode-3 sensor $S^T_{\sigma\varepsilon}(3, x)$ is given in Fig. 6. It is seen that up to about 1 kHz good modal discrimination is predicted and represents well the amplitude of the target mode. A small glitch in the response around 850 Hz is seen to be larger for the sensor designs $S^T_n(3, x)$ and $S_h(3,x)$ is an indication that $S^T_{\sigma\varepsilon}(3, x)$ is the best design. Although apart from this the responses appear to be similar.

Two other variations of the sensor $S^T_{\sigma\varepsilon}(3, x)$ were considered: one where the PVDF sensor has no response to bending in the y-direction (that is $e^0_{32} = 0$ in Eq. (24)—essentially a 1-D sensor), and one where there was a sensor placement error of -1.1 mm in the x-axis. It can be seen that both these introduce errors in the response that are larger than those due to different sensor design methods shown in part (a) of the figure. These errors will be discussed further when the experimental results are presented.

7. Experimental implementation

7.1. Beam fabrication and assembly

The non-uniform thickness beam was fabricated from one continuous component being machined from a larger block of stainless steel. Other options of implementing the change in thickness by adjoining additional sections (as considered in Ref. [14]) would make the system more complex to model due incomplete transfer of strain over a bonding interface, or non-uniform strain transfer if components such as rivets, for example, were used.

The simply supported boundary condition was implemented by supporting each end of the beam in steel end block. V-grooves were machined in each end block and similar smaller grooves in each beam end. A 1.5 mm diameter steel wire was trapped in between the beam and the support, located in the grooves, to assimilate a hinged joint. One support was moveable, and adjusted to allow the smallest compression necessary to support the beam and introduce the minimum of rotational stiffness or in-plane compression of the beam.

The V-grooves were lubricated with graphite to reduce friction. One problem was that the machined beam had a small amount of warping due to the machining of the thin-sections from a larger block. This was minimised by reducing the material thickness in small steps alternately from each face to reduce the warping introduced as the balance of internal stresses was relieved. For this reason a slightly higher compression force was required between the end supports.

7.2. Piezoelectric actuator implementation

Near one beam end two actuators are placed towards the beam free edges so as to leave the inner section free for the sensor placement. Both actuators were electrically driven in unison. Each actuator was comprised of two piezoelectric elements of dimensions $40 \times 5\,mm^2$ with thickness $250\,\mu m$, and were collocated on each side of the beam. When the elements of each actuator are driven electrically in anti-phase each actuator excites the beam in bending. The elements are bonded to the beam using Araldite-D + HY956 (Ciba & Geigy) in a 5:1 ratio. Fine silk gauze was used as a spacing material to ensure electrical isolation between the beam and the electrode and to ensure an even thickness of the bonding layer, which was about $25\,\mu m$. A 2 mm section of the upper electrode was previously separated to make a connection to the underside electrode by spluttering. Given the thinness of the actuators the mechanical loading on the beam is negligible and not considered in the FEA model.

7.3. PVDF sensor implementation

Forty-micrometer thick biaxially oriented PVDF material was used to construct the sensors. Each sensor section was fabricated in the following way. First, a PVDF strip assembly is made from which one sensor section outline will be transferred and cut. Electrical connections are made to the underside the sensor strip by affixing a thin strip of plastic backed thin copper foil with electrically conductive tape and reinforcing the connection with silver conductive paint. 3M *Double Coated Tape 9570* (70 μm thick) is then applied to the cover the entire strip that will subsequently bond the underside of the PVDF sensor to the beam. Next, the sensor outline for each section (correctly scaled in length and maximum width) is printed on to tracing paper using an Ink Jet printer. The outline is transferred to the upper electrode by temporarily applying non-deformable, no residue, transparent tape to the printed-paper surface, which is then permanently applied to the upper electrode (the electrical connection is made through a small window in the tape). The sensor is then trimmed to the outline, and satisfactory results were achieved cutting using a sharp scalpel-type knife along a straight edge or by free hand. The estimated accuracy of the cutting process is within one-third of a millimetre.

Particular care should be taken as the surface electrodes of the PVDF are very thin (in the region of 0.03 μm [15]) and easily damaged. Thus extreme care should be taken in the handing of the material—protecting contact from abrasion with all but soft surfaces. Also, contact with sharp objects, and in particular test probes, is likely to dent or score the surface [14]. Contact should be achieved by smooth soft conductive surfaces. Any damage may not easily visible but can have a detrimental effect to the sensor performance.

The measurement of the capacitance of each sensor section is a good way of testing the integrity of the both the electrical contacts and the electrodes. A capacitance meter with a resolution of at least 10 pF is needed. The approximate capacitance of each sensor section can be calculated as a check, and also the similarity of capacitance between similarly sized-sections can be verified. This is important in detecting contact failures where capacitive coupling may result in which case an electrical signal can usually still be registered, with a similar frequency response—albeit at a different level. This is particular important when electrically combining sensor outputs. In the experimental system the relative error capacitances of the individual sections was less than 2%.

After affixing the sections to the beam, taking care in their positioning, the electrical connections are made to upper electrode using silver conductive paint and to underside electrode by rapid soldering to the copper foil. Fig. 7 shows the full five-section mode-3 sensor applied to the beam surface. The required polarity of each sensor section was achieved by the appropriate electrical connection to each section.
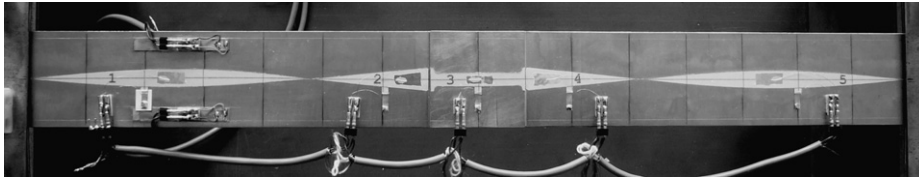
Fig. 7. The beam system showing the five-section mode-3 PVDF sensor and the actuators. (The thin wires providing electrical connections to the sensor are barely distinguishable.)
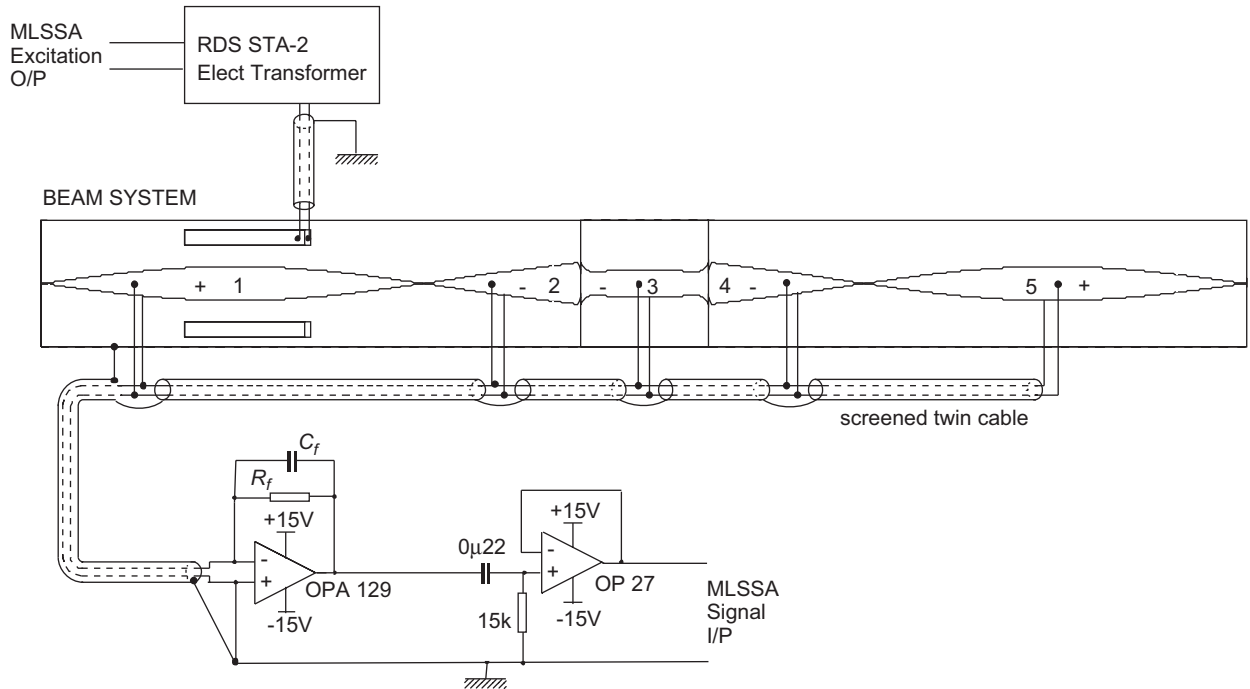

Fig. 8. A schematic diagram of the experimental system showing the beam actuation and the sensing circuitry comprising of charge amplifier (OPA129) and a high-pass filter (OP27). The numbered sensor sections are shown to scale and their connection polarity is denoted.

7.4. Experimental set-up, sensing circuitry and signal processing

A schematic of the experimental set-up is shown in Fig. 8. The beam actuators are driven with a voltage of ± 5 V through screened cables to avoid interference with the vibration sensing. The low voltage is due to the thinness of the actuators used (the strain being dependent upon the electric field and not the applied voltage).

A disadvantage of PVDF sensors is the small electrical output signal and it is necessary to use a sensitive charge amplifier with high input impedance and low input bias current. The charge amplifier circuit used here is also shown in Fig. 8. The values of C_f and R_f determine the conversion of charge sensitivity and the lower cut-off frequency (in this case: 2 Hz) [16]. In addition, to remove any d.c. offsets from the amplifier response, this is followed by a high-pass filter with cut-off at 2 Hz. The output voltage of the of the amplifier is [16]

$$V_{\text{out}} = \frac{-\Delta Q}{C_f}, \tag{36}$$

where C_f is the feedback capacitance and ΔQ the charge output of the sensor. This is for an ideal charge amplifier and the sources of error and dependence on other system capacitances and resistances are discussed in Ref. [17].

It is also necessary to adequately screen the sensor cables and the charge amplifier circuitry to eliminate interference. A coherent grounding system should be used, avoiding ground loops and separating supply and signal earths as much as possible. Due to the extremely small electrical charges and current involved, good electrical isolation of the sensor electrodes and associated connections is required; even a resistance in the order of mega-ohms will effectively be a "short".

The frequency response of the sensors was achieved using *MLSSA* [18], a system based on maximum length sequences [19]. In brief, a two-valued bipolar signal of length 2^{14} is used to drive the system. The sequence has an auto-correlation function that is effectively a delta function. The signal was sampled with a 12-bit ADC. The auto-scaling function of the *MLSSA* application and the continuous nature of the excitation signal ensure at least a resolution of 11-bits is achieved. A sampling frequency of 8 kHz was used, and a frequency resolution of 0.49 Hz is achieved. Only a frequency range to 1 kHz was considered for the experimental results. One hundred frequency record averages were used, except for the individual response of sensor Section 3 where 200 averages were used due to the lower signal level.

8. Experimental results

The electric charge outputs of the individual sensor sections for the experimental system are given in Fig. 9 along with the predicted responses from the numerical model. Unwrapped phase is used and a pertinent number of integer multiples of π are added to the experimental results to counter the phase offset due to the low-frequency noise in the experimental system. As the gain of the amplifier depends on the total capacitance of the sensor sections connected and the capacitance of the cable and op-amp input, the magnitude of the measured results is adjusted accordingly. Good agreement is seen in general, especially for sensors 2 and 5. For sensors 1 and 4 discrepancies in the frequencies of the anti-resonances from the numerical model are seen. Sensor 3 shows significant error at frequencies below 200 Hz. In the region of 850 Hz three closely spaced resonances are seen in place of the single resonance predicted for all sections. This is thought to be due to the lack of integrity of the boundary conditions.

In Fig. 10 the response of the complete sensor (all the sections electrically combined as shown in Fig. 8) is also shown. Considering the individual sensor responses in Fig. 9 it is evident that good modal discrimination has been achieved and that there is generally faithful measurement of the true modal amplitude up to about 700 Hz. The errors above this frequency are expected due to similar errors in the individual section responses. With reference to Table 1, the glitches at 120 and 500 Hz correspond to modes (2,1,0) and (4,1,0), and have similar features in the response at these frequencies to those predicted due to sensor placement error and/or reduced cross-axis sensitivity (see Fig. 6). It is suggested that transference of strain between the beam surface and the PVDF material is not as faithful across its width as along the length of the sensor due to the difference of dimension of the contiguous tape interface. These possible error sources are discussed further below.

Also shown in Fig. 10 is the summation of the individual section magnitude and phase-corrected responses shown in Fig. 9. It is now seen that the errors at 120 and 500 Hz are now large spikes that are only about 10 dB smaller than the peak amplitude. One reason for the difference between the sum of the individual responses and the combined sensor is thought to be that when connected individually, the electrical loading effects for each sensor section alter slightly. This interacts with the electrical loading of the charge amplifier and the cables to slightly change the poles and/or zeros of the overall response. When the individual responses are combined these slight pole-zero misalignments result in spikes in the frequency response. This effect is not considered further here.

9. Discussion

Earlier work by the author [3] used a Rayleigh–Ritz model of the non-uniform thickness beam, which as discussed is not valid in the region of the discontinuities in thickness. This is because in this case the apparent surface strain is the product of the beam thickness and the second-order spatial derivative of displacement.
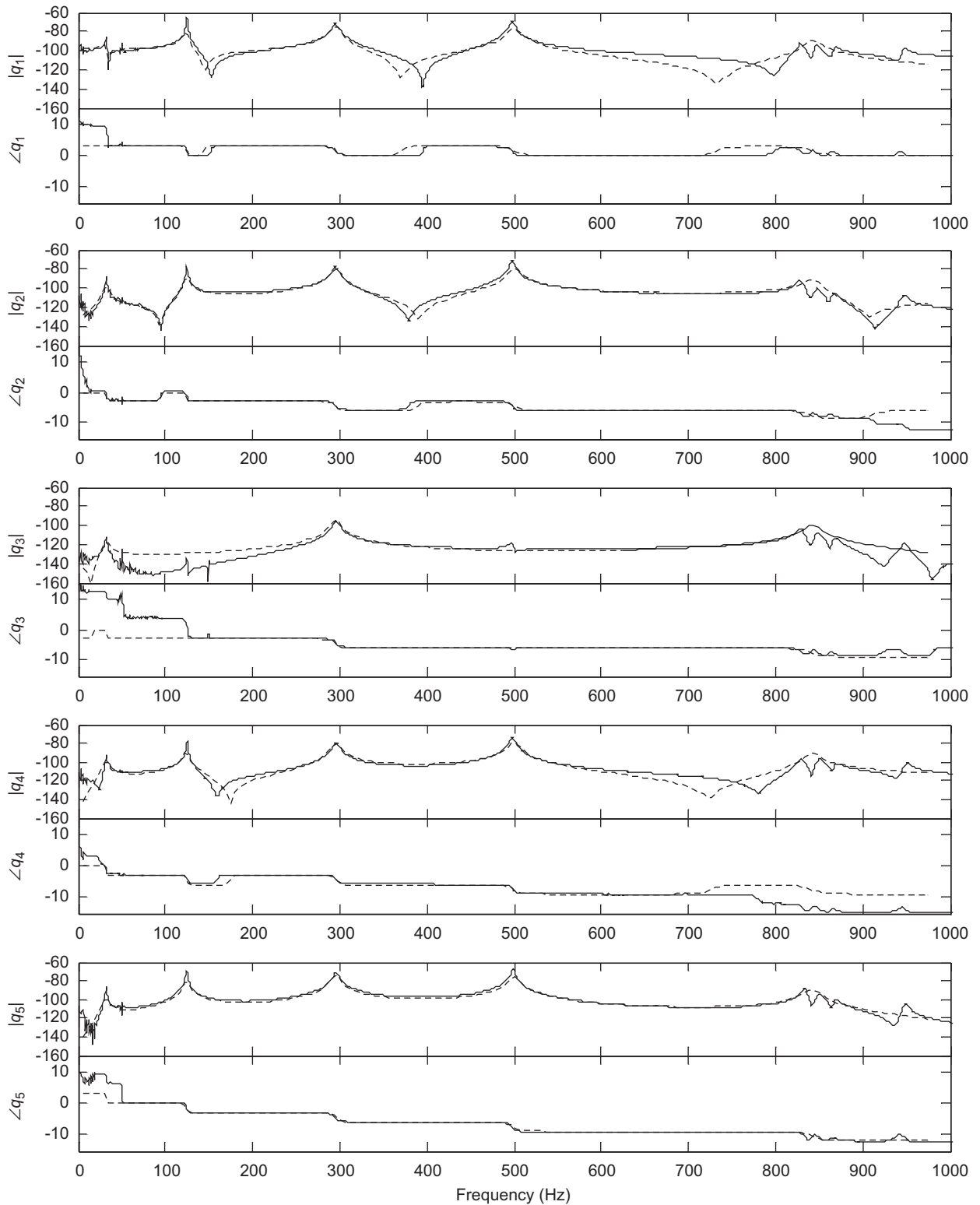
Fig. 9. Bode plot experimental responses (in dBs and unwrapped phase in radians) of the charge output of each sensor section, q_1 to q_5 (—), compared with their predicted responses ($\cdots$).
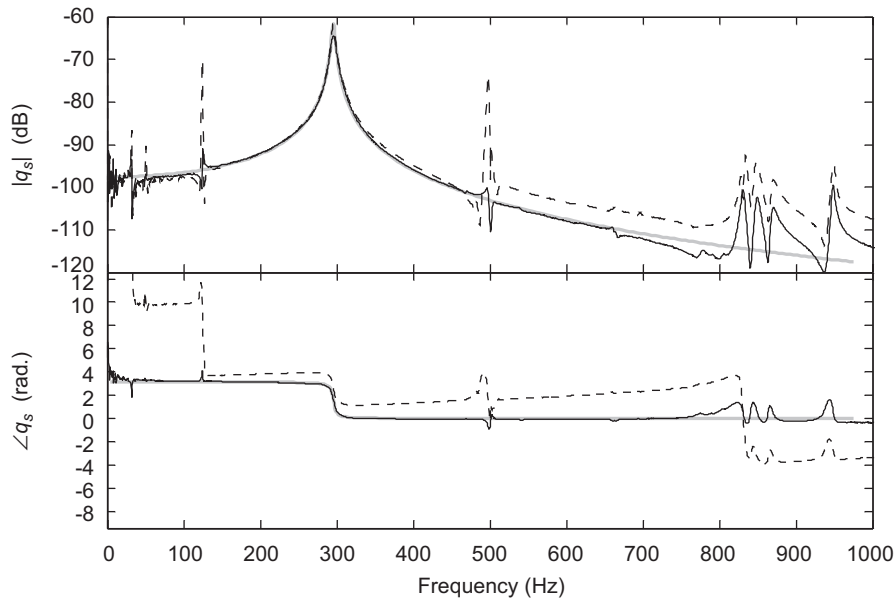
Fig. 10. Bode plot response of the complete experimental five-section sensor (—) and the response synthesised by summing the individual section responses shown in Fig. 9 (···). The true amplitude of mode-3 is shown arbitrarily scaled (▬).

To accommodate the discontinuities a large number of basis functions (a half-sine series) were required, but an effect equivalent to Gibb's phenomenon in Fourier analysis was seen in the region of the discontinuity and thus in the sensor profile as this was the basis for the sensor design. However, it is seen in Fig. 4 that no discontinuity exists in the strain on the beam surface or on any inner plane. Some limited success of modal discrimination for a similar non-uniform thickness beam was achieved but to a much lesser quality than reported here [14] despite significant differences in the shape of the mid-sensor sections.

There are many possible errors in the both modelling and application of PVDF sensors. Obviously the sensors should be implemented with the precise shape and location as modelled, however not all errors are attributed to these. Here it has been shown that placement errors of about 0.3% of the beam length are responsible for errors in the frequency response. Clark and Burke [4] also reported this as an explanation for experimental errors using a similar beam and placement error size. However, errors are also possible from the modelling of the beam and sensor as a 1-D system. From Table 1 it is seen that higher order modes in the y-direction appear early on in the modal order and cannot be simply disregarded due to low-frequency consideration. Apart from producing differences in modal frequencies of the $(*,1,0)$ modes a 1-D model will also produce two types of error in the PVDF sensor. First, a variation of the bending in the x-axis across the sensor width, and secondly, if this variation has a non-zero second derivative then bending in the y-axis for which the sensor will produce a separate response component. The deterioration of the response of an apparently good sensor due to ignoring these has been illustrated in Ref. [3]. However, due to the suspected reduced mechanical coupling between the beam surface and the sensor across its width the effective value of e_{32}^0 would be between 0 and e_{32}^0 and so this error may not be so pronounced. Even so, it is seen to lead to errors that appear similar to those for sensor placement errors.

In Ref. [3] the consequence of modal detection using PVDF sensors is discussed for a uniform thickness beam using second spatial derivatives, which in this case is equivalent to surface strain. It is shown that there is a natural amplification in the detected amplitude of higher order modes implicit in sensing in this domain. Thus, the below-resonance residuals of higher order modes are much more significant and the sensor modal discrimination must be better to achieve the same modal rejection as when using displacement, velocity or acceleration sensing. In the case of a uniform thickness beam this factor is the wavenumber of the mode shape squared. This analysis cannot be extended directly to non-uniform thickness beams but can be applied qualitatively to suggest that a similar effect occurs.

One further disadvantage of detection using strain sensors is seen with reference to Fig. 5, where the normalised displacement, second spatial derivative and surface strain for the mode-3 are shown together. It is seen that for relatively small deviations in the displacement, much larger deviations are seen for the other two parameters. It is thus possible to conceive of a uniform thickness beam that has a small defect that is insignificant in the displacement mode shape, but significant, for example, in the surface strain mode shape and thus will cause errors in the application of strain sensors. Thus strain sensing is more sensitive than displacement sensing to possibly unknown defects in surfaces to which they are applied. For this reason strain modes are widely used in fault detection (for example see Ref. [20]).

Sensors to detect combinations of modes could be made from combining the individual shape weighting functions, correctly scaled, for each mode to form a radiation mode sensor as would be required for ASAC. It is noted that individual structural mode sensing is more stringent than radiation mode detection. This is because radiation modes are usually combinations of structural modes with orders of the same parity. Here, the modal discrimination errors are seen to correspond to the same parity of the design mode. These error components may be masked by other desired modal components with similar parity, or the modal amplitudes could be adjusted to compensate for the predicted error components.

Finally, it is noted that the strain-energy-based orthogonality condition developed in this paper cannot be applied to non-uniform thickness plates. As an example, assume a simply supported plate with a thickness function $h(x,y)$ that in the x-axis is equal to the function $h(x)$ of the beam considered here, but has uniform thickness in the y-axis. Even though displacement field could be expressed as the product of separable plate mode shapes ϕ_m^P and ϕ_n^P in x and y, respectively, as

$$W^P(x,y) = \sum_{m,n} A_{mn}\phi_m^P(x)\phi_n^P(y), \tag{37}$$

the mode shapes in the x-direction are not the same as those for a non-uniform thickness beam, that is $\phi_m^P(x) \neq \phi_m(x)$. This is illustrated in Ref. [14]. This is caused by the greater effect of the coupling between plate flexion in the two axes (caused by Poisson's effect) due to either the dimension of the plate in the y-direction being more significant than for the beam considered here, and/or boundary conditions other than free–free conditions along the boundaries in the x-direction.

10. Conclusions

The design of PVDF strain sensors for modal detection of a simply supported non-uniform thickness beam has been considered. Traditional kinetic-energy-based orthogonality conditions, based on displacement or its temporal derivatives, are not applicable and a strain-energy-based orthogonality condition was developed. This was done in both terms of spatial derivatives and the surface and the internal strain (and stress) of the beam. The orthogonality condition is approximate, but results from a numerical model demonstrated good modal discrimination although errors were greater for the two lowest modal orders. The design procedure preceded using 1-D approximations of the beam and the PVDF sensor; however the numerical model was capable of fully representing the system. It was shown that modelling the beam system and the PVDF sensor as 1-D entities resulted in modelling errors. These are of similar significance to errors in the positioning of the sensors that have been previously reported. Thus, errors in implementing such systems could be attributed to a number of sources.

A modal sensor was implemented experimentally for a non-uniform thickness beam with a central section augmented in thickness by a factor of two. The results corresponded well with those predicted by the numerical model. The upper frequency range of the modal detection was in practice limited by possible errors in the boundary conditions.

Finally, despite the advantages of PVDF sensors over other transducers in practical systems the disadvantages of strain sensing instead of displacement (or velocity, or acceleration) sensing was discussed. It was also shown that the orthogonality condition cannot be extended for application to non-uniform thickness plates.

Acknowledgements

Appendix A

This analysis follows closely to that of Dimitriadis et al. [13], but is derived here for the general case. The actuator is defined in the main text. Assuming a plate of dimensions L_x and L_y with a rectangular actuator with position defined by the coordinates x_1, x_2, y_1, y_2, the moment couples along each edge are defined by

$$m_x = m_y = C_0 \varepsilon_{\mathrm{pe}}[H(x - x_1) - H(x - x_2)][H(y - y_1) - H(y - y_2)] \tag{A.1}$$

where H is the unit step function. The piezoelectric strain plate coupling term, C_0, and the induced strain in the piezoceramic elements, $\varepsilon_{\mathrm{pe}}$, are defined by

$$C_0 = -E_p \frac{1 + v_{\mathrm{pe}}}{1 - v_p} \frac{P}{1 + v_p - (1 + v_{\mathrm{pe}})P} \frac{2}{3}(h/2)^2, \quad \varepsilon_{\mathrm{pe}} = \frac{d_{31}}{t} V, \tag{A.2a,b}$$

where

$$P = \frac{-E_{\mathrm{pe}}}{E_p} \frac{1 - v_p^2}{1 - v_{\mathrm{pe}}^2} K, \quad K = \frac{3t(h/2)(h + t)}{2((h/2)^3 + t^3) + 3(h/2)t^2}. \tag{A.3a,b}$$

Here E is the Young's modulus, v the Poisson's ratio, d_{31} a piezoelectric strain constant, h the plate thickness, t the thickness of the actuator, and V the applied electric driving voltage. The subscripts p and pe denote the plate and the piezoelectric element, respectively.

The equation of motion of the plate may be written using thin plate theory. This shows the effect of the actuator induced moments, m_x and m_y, on the internal plate bending moments, M_x, M_y and M_{xy}, and is

$$\frac{\partial^2(M_x - m_x)}{\partial x^2} + 2\frac{\partial^2 M_{xy}}{\partial x \partial y} + \frac{\partial^2(M_y - m_y)}{\partial y^2} + m''(x, y)\ddot{W} = 0, \tag{A.4}$$

where m'' is the plate area density. The moments can be transferred to the right-hand side, thus

$$\frac{\partial^2 M_x}{\partial x^2} + 2\frac{\partial^2 M_{xy}}{\partial x \partial y} + \frac{\partial^2 M_y}{\partial y^2} + m''(x, y)\ddot{W} = \frac{\partial^2 m_x}{\partial x^2} + \frac{\partial^2 m_y}{\partial y^2}. \tag{A.5}$$

However, when the equation is expressed in terms of displacement, the derivation deviates from that of Dimitriadis et al. as for a non-uniform thickness plate the plate flexural rigidity, EI (where I is the second moment of area, and EI is equivalent to D), is a spatial variable. An equation with a fourth-order differential operator cannot be formed, but instead the general case gives

$$\frac{\partial^2}{\partial x^2}\left[EI(x,y)\frac{\partial^2 W}{\partial x^2}\right] + 2\frac{\partial^2}{\partial x \partial y}\left[EI(x,y)\frac{\partial^2 W}{\partial x \partial y}\right] + \left[EI(x,y)\frac{\partial^2 W}{\partial x^2}\right] + m''(x,y)\ddot{W} = \frac{\partial^2 m_x}{\partial x^2} + \frac{\partial^2 m_y}{\partial y^2}. \tag{A.6}$$

This may be dealt with by applying an analysis to a similar problem as considered by Cremer and Heckl [5]. A general equation of motion may be written using the differential operator L, which is defined by comparison with the previous equation as

$$L[W] - m''(x,y)\omega^2 W = \frac{\partial^2 m_x}{\partial x^2} + \frac{\partial^2 m_y}{\partial y^2}. \tag{A.7}$$

For a conservative system, each set of eigenfrequencies and eigenfunctions must satisfy the following condition:

$$L[\phi_{mn}(x,y)] - m''(x,y)\omega_{mn}^2\phi_{mn}(x,y) = 0. \tag{A.8}$$

Expressing the displacement field as the sum of an infinite series of eigenfunctions and corresponding amplitudes, A_{mn}, by

$$W = \sum_{m,n} A_{mn}\phi_{mn}(x,y). \tag{A.9}$$

Inserting Eq. (A.9) into Eq. (A.7) yields

$$\sum_{m,n} A_{mn}\{L[\phi_{mn}(x,y)] - m''(x,y)\omega^2\phi_{mn}(x,y)\} = \frac{\partial^2 m_x}{\partial x^2} + \frac{\partial^2 m_y}{\partial y^2} \tag{A.10}$$

and now subtracting Eq. (A.8) from the result, the differential operator vanishes, and multiplying both sides by $\phi_{m'n'}$ and integrating over the entire surface and applying orthogonality, only a non-zero left-hand side is obtained when $mn = m'n'$, thus

$$A_{mn}(\omega_{mn}^2 - \omega^2)\int_S m''(x,y)\phi_{mn}^2(x,y)\,\mathrm{d}s = \int_S \phi_{mn}(x,y)\left(\frac{\partial^2 m_x}{\partial x^2} + \frac{\partial^2 m_y}{\partial y^2}\right)\mathrm{d}S. \tag{A.11}$$

Choosing the first term on the right-hand side of the equation as an example

$$\int_S \phi_{mn}(x,y)\frac{\partial^2 m_x}{\partial x^2}\mathrm{d}S = C_0\varepsilon_{\mathrm{pe}}\int_S \phi_{mn}(x,y)[\delta'(x-x_1) - \delta'(x-x_2)][H(y-y_1)H(y-y_2)]\,\mathrm{d}S \tag{A.12}$$

and after some algebraic manipulation and solution this produces

$$\int_S \phi_{mn}(x,y)\frac{\partial^2 m_x}{\partial x^2}\,\mathrm{d}S = C_0\varepsilon_{\mathrm{pe}}\int_{y_1}^{y_2}\left(\frac{\partial\phi_{mn}(x_2,y)}{\partial x} - \frac{\partial\phi_{mn}(x_1,y)}{\partial x}\right)\mathrm{d}y = C_0\varepsilon_{\mathrm{pe}}G_{mn}^x(x_1,x_2), \tag{A.13}$$

where the function G_{mn}^x is defined for convenience. Similarly the second term is resolved as

$$\int_S \phi_{mn}(x,y)\frac{\partial^2 m_y}{\partial y^2}\,\mathrm{d}S = C_0\varepsilon_{\mathrm{pe}}\int_{x_1}^{x_2}\left(\frac{\partial\phi_{mn}(x,y_2)}{\partial y} - \frac{\partial\phi_{mn}(x,y_1)}{\partial y}\right)\mathrm{d}x = C_0\varepsilon_{\mathrm{pe}}G_{mn}^y(y_1,y_2). \tag{A.14}$$

Using G_{mn}^x and G_{mn}^y, Eq. (A.12) may be now used to define the coefficients of the modes of the displacement field

$$A_{mn} = \frac{C_0\varepsilon_{\mathrm{pe}}[G_{mn}^x(x_1,x_2) + G_{mn}^y(y_1,y_2)]}{\Lambda_{mn}(\omega_{mn}^2 - \omega^2)}, \tag{A.15}$$

where the modal mass Λ_{mn} is defined as

$$\Lambda_{mn} = \int_S m''(x,y)\phi_{mn}^2(x,y)\mathrm{d}S. \tag{A.16}$$

References

[1] C.R. Fuller, S.J. Elliott, P.A. Nelson, *Active Control of Vibration*, Academic Press, New York, 1996.
[2] N. Tanaka, S.D. Snyder, C.H. Hansen, Distributed parameter modal filtering using smart sensors, *Journal of Vibration and Acoustics* 118 (1996) 630–640.
[3] D. K. Anthony, P. Cobo, Measuring the vibrational modes of non-uniform beams with PVDF sensors using a strain energy orthogonality condition, *Proceedings of the 2004 International Conference on Noise and Vibration Engineering (ISMA 2004)*, 2004, pp. 115–129.
[4] R.L. Clark, S.E. Burke, Practical limitations in achieving shaped modal sensors with induced strain materials, *Journal of Vibration and Acoustics* 118 (1996) 668–674.

 [5] M. Heckl, L. Cremer, *Structure-Borne Sound*, Springer, Berlin, 1987.
 [6] W. Weaver, S.P. Timoshenko, D.H. Young, *Vibration Problems in Engineering*, Wiley, New York, 1989.
 [7] A.C. Ugural, *Stresses in Plates and Shells*, McGraw-Hill, New York, 1999.
 [8] C.K. Lee, F.C. Moon, Modal sensors/actuators, *Journal of Applied Mechanics* 57 (1990) 434–441.
 [9] Y. Gu, R.L. Clark, C.R. Fuller, A.C. Zander, Experiments on active control of plate vibration using piezoelectric actuators and polyvinylidene fluoride (PVDF) modal sensors, *Journal of Vibration and Acoustics* 116 (1994) 303–308.
[10] A. Preumont, *Vibration Control of Active Structures: An Introduction*, Kluwer Academic, Dordrecht, 2002.
[11] ANSYS 9.0, ANSYS Inc., Canonsburg, USA. ⟨www.ansys.com⟩.
[12] MATLAB 7.0, The MathWorks Inc., Natick MA. ⟨www.mathworks.com⟩.
[13] E.K. Dimitriadis, C.R. Fuller, C.A. Rogers, Piezoelectric actuators for distributed vibration excitation of thin plates, *Journal of Vibrations and Acoustics* 113 (1991) 100–107.
[14] D. K. Anthony, Sensores para medir independientemente modos estructurales de barras y placas no-uniformes para aplicación al control-activo-acústico-estructural, Project Report GR/AMB/0736/2004—Comunidad de Madrid, 2006 (in Spanish).
[15] Personal communication. *Supplier of PVDF*. Goodfellow Cambridge Ltd., Huntingdon, UK. February 2005.
[16] Burr-Brown Corporation, *OPA129 Ultra-low Bias Current Difet Operational Amplifier, Data Sheet*. 1994.
[17] R. Pallàs-Areny, J.G. Webster, *Sensors and Signal Conditioning*, second ed., Wiley, New York, 2000.
[18] D. Rife, *MLSSA: Maximum-length Sequence System Analyser. Reference Manual, Version 10.0A*, DRA Laboratories, 1996.
[19] D. Dife, J. Vanderkooy, Transfer-function measurements with maximum length sequences, *Journal of the Audio Engineering Society* 37 (6) (1989) 419–444.
[20] A.K. Pandey, M. Biswas, M.M. Samman, Damage detection from changes in curvature mode shapes, *Journal of Sound and Vibration* 145 (2) (1991) 321–332.